Oil & Natural Gas Technology

DOE Award No.: DE-FE0013889

Quarterly Research Performance Progress Report (Period ending 01/31/2016)

THCM Coupled Model For Hydrate-Bearing Sediments: Data Analysis and Design of New Field Experiments (Marine and Permafrost Settings)

Project Period (10/1/2013 to 09/30/2016)

Submitted by:

Marcelo Sanchez Project PI

Texas A&M University
DUNS #: 847205572
College Station, TX
979-862-6604
msanchez@civil.tamu

Prepared for:
United States Department of Energy
National Energy Technology Laboratory
Submission date: 02/05/2016

Office of Fossil Energy

DISCLAIMER

“This report was prepared as an account of work sponsored by an agency of the United States Government. Neither the United States Government nor any agency thereof, nor any of their employees, makes any warranty, express or implied, or assumes any legal liability or responsibility for the accuracy, completeness, or usefulness of any information, apparatus, product, or process disclosed, or represents that its use would not infringe privately owned rights. Reference herein to any specific commercial product, process, or service by trade name, trademark, manufacturer, or otherwise does not necessarily constitute or imply its endorsement, recommendation, or favoring by the United States Government or any agency thereof. The views and opinions of authors expressed herein do not necessarily state or reflect those of the United States Government or any agency thereof.”

ACCOMPLISHMENTS

The experimental study of hydrate bearing sediments has been hindered by the very low solubility of methane in water (lab testing), and inherent sampling difficulties associated with depressurization and thermal changes during core extraction. This situation has prompted more decisive developments in numerical modeling in order to advance the current understanding of hydrate bearing sediments, and to investigate/optimize production strategies and implications. The goals of this research is to addresses the complex thermo-hydro-chemo-mechanical THCM coupled phenomena in hydrate-bearing sediments, using a truly coupled numerical model that incorporates sound and proven constitutive relations, satisfies fundamental conservation principles. This tool will allow us to better analyze available data and to further enhance our understanding of hydrate bearing sediments in view of future field experiments and the development of production technology.

ACCOMPLISHED

The main accomplishments for this first period address Tasks 5, 6 and 7 of the original research plan, and include:

- Update of constitutive equations.
- Update of THCM-Hydrate.
- Numerical analyses.
- Incorporation of additional THCM-Hydrate code modifications.
- Production Optimization of Future Field Studies.

Training

The training of the two PhD students working in this project has continued during this period. Mr. Xuerui (Gary) Gai was hired at the start of the project and his activities have been related to the use of code "THCM-Hydrate"; which is the numerical tool under development in this project. His research has focused on the mechanical modeling of Hydrate Bearing Sediments (HBS). Mr. Mehdi Teymouri was hired at the beginning of the second year of the project. His research has focused on modeling numerical and analytical methods in hydrates research. He is also working in sand production when producing gas from methane hydrate reservoirs. Both students have progressed positively with their coursework at their respective universities.

Literature review

The literature review (Task 2) was completed in a previous period.

Update of Update of THCM-Hydrate

The update of the constitutive laws for hydrate-bearing marine sediments and HBS in the permafrost (i.e. Task 3) was completed in a previous period.

Close-form analytical solutions

The review on the main governing evolution laws, parameters, dimensionless ratios and simplifying assumptions for HBS dissociation (i.e. Task 4) was completed in the previous period.

Numerical analyses

The numerical analyses to solve field production experiments as boundary value problems have continued in this period.

The study of HBS during dissociation performed in this period is reported in page 6.

In parallel progresses have been made in the modeling of methane production experiments from pressurized cores. Large scale models are also being developed to simulate real production tests. Finally, the modeling of sand production during HBS depressurization is another topic in which progress has been made in this period.

Plan - Next reporting period

We will advance analytical and numerical fronts to enhance our code to solve coupled THCM problems involving with HBS, with renewed emphasis on simulating the natural processes under *in-situ* conditions and gas production. Special emphasis will be placed on issues associated with sand production

.

Milestones for each budget period of the project are tabulated next. These milestones are selected to show progression towards project goals.

	Milestone Title Planned Date and Verification Method	Actual Completion Date	Comments
Title Related Task / Subtasks Planned Date Verification method	Complete literature review 2.0 / 2.a March 2014 Report	March 2014	Completed
Title Related Task / Subtasks Planned Date Verification method	Complete updated Constitutive Equations 2.0 / 2.b & 2.c June 2014 Report (with preliminary validation data)	July 2014	Completed
Title Related Task / Subtasks Planned Date Verification method	Validate new THCM constitutive equations 3.0 / 3.a, 3.b & 3.c September 2014 Report (with first comparisons between experimental and numerical results)	September 2014	Completed
Title Related Task / Subtasks Planned Date Verification method	Complete close-form analytical solutions 4.0 / 4.a & 4.b February 2015 Report (with analytical data)	February 2015	Completed
Title Related Task / Subtasks Planned Date Verification method	Complete numerical analyses 5.0 / 5.a, 5.b & 5.c July 2015 Report (with analytical and numerical data)	July 2016	Progressing as planned
Title Related Task / Subtasks Planned Date Verification method	Complete THCM-Hydrate code modifications 6.0 / 6.a June 2015 Report (with numerical data)	June 2016	Progressing as planned
Title Related Task / Subtasks Planned Date Verification method	Complete production optimization 7.0 / 7.a, 7.b, 7.c, 7.d & 7.e September 2015 Report (with numerical data)	September 2016	Progressing as planned

BEHAVIOR OF HBS DURING DISSOCATION

1 Introduction

Hydrate dissociation experiments under stress have allowed gaining a better understanding on the mechanical response of sediments when the presence of hydrates vanish. Two types of tests involving hydrate dissociation conducted under triaxial and oedemetric loading conditions are briefly discussed in this report.

Hyodo et al. (2014) adopted a temperature-controlled high pressure triaxial apparatus to mimic the formation and dissociation of methane hydrate in the deep seabed. This device was used to conduct a series of triaxial compression tests on synthetic HBS samples under various conditions. Toyoura sand was chosen as the host material to prepare samples with a similar porosity (i.e., ~40%), and with S_h ranging from ~37% to 53%. Three experiments were selected in this work for the numerical simulations, namely: two triaxial tests at which hydrate dissociation was induced at two different initial axial strains (i.e., ε_a=1%, and ε_a=5%), and a third one in which the sample was subjected to shearing after the hydrates dissociated fully. These tests were conducted under isotropically consolidated specimens, at an effective confining stress σ'_c=5 MPa, and under drained conditions. Figure 1a presents the main experimental results in terms of axial strains against deviatoric stress and also against volumetric strains. In one of the dissociation tests, the specimen was firstly sheared up to q≈8.4 MPa (i.e., at ε_a=1%), then dissociation was induced at constant stress conditions and, after fully dissociation, the shearing continued up to ε_a=20%. A similar procedure was followed for the other dissociation test, but the maximum deviatoric load in this cases was q≈12 MPa (i.e., at ε_a=5%). The responses observed under these test conditions are quite different. In the first test, the deviatoric stress after hydrate dissociation was smaller than the shear strength of the dissociated sediment, therefore a tendency to harden was observed in the subsequent shearing. However, in the second sample (i.e., dissociation induced at ε_a=5%) the deviatoric stress was higher than the strength of the dissociated sample. In consequence, stress-softening was observed during the hydrate dissociation stage, with a tendency of the deviatoric stress to decrease and reach the maximum deviatoric stress observed in the already dissociated sample. More details about these tests and the associated modeling are presented in Section 4.1.

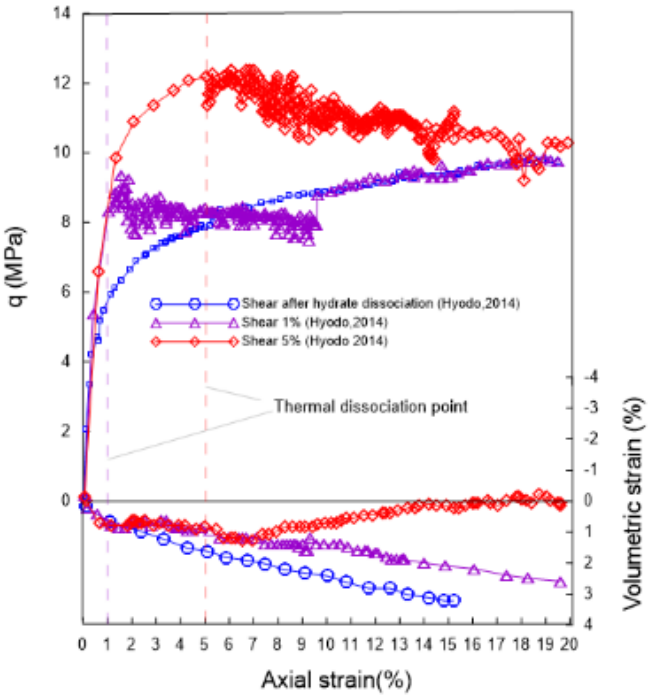

a)

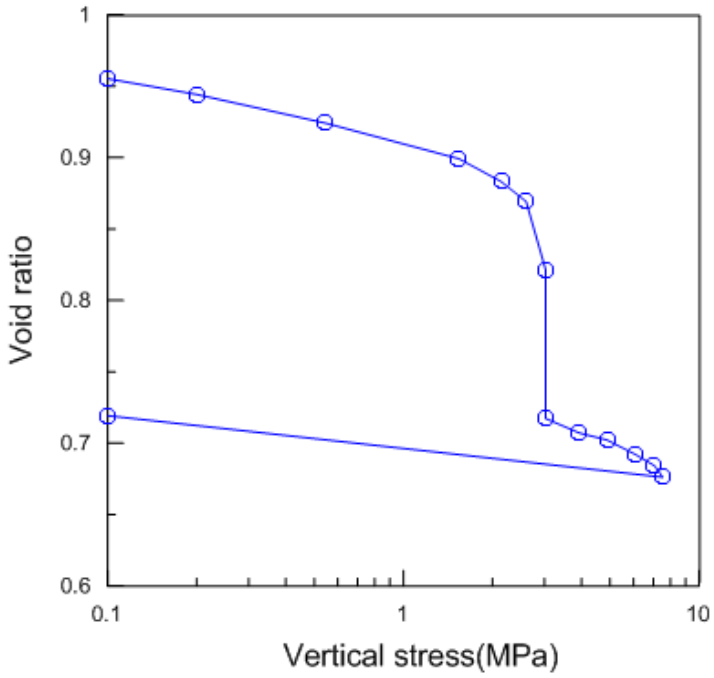

b)

Figure 1. a) Experimental results for drained triaxial tests involving hydrate dissociation (Hyodo et al., 2014), b) behavior of a natural HBS subjected to loading and dissociation under stress at oedemetric conditions (Santamarina et al., 2015).

The other set of experiments modeled in this paper corresponds to the tests reported by Santamarina et al. (2015). Two natural core samples were extracted from the Nankai Trough, offshore Japan, using the Pressure Core Characterization Tools (PCCT, Santamarina et al., 2012). The tested cores were predominantly sandy- and clayey-silts, but also contained some silty-sands. Hydrate saturation ranged from 15% to 74%, with significant concentrations in the silty-sands samples. The PCCT was able to maintain the HBS cores stable at field conditions. After retrieval, the cores were loaded under oedometric conditions, allowing hydrate dissociation under stress. The mechanical behavior of the HBS specimens before, during and after dissociation was recorded. Figure 3b shows the results of a typical test in the 'effective stress chamber' (i.e., the sample coded as 'core-10P', with an initial S_h=74%). Prior to hydrate dissociation, the specimen was loaded up to an applied effective vertical stress σ'_v=3 MPa, then hydrate dissociation was induced via depressurization maintaining the effective stress constant. Once the hydrates were fully dissociated, the specimen was loaded up to σ'_v=9 MPa, and it was unloaded afterwards. A significant volumetric collapse-compression deformation was observed during dissociation under load. This test and another one with lower hydrate dissociation (i.e., S_h=18%) are modeled and discussed in Section 4.2.

2. Discussion on the experimental observations

From the previous sections it can be concluded that the behavior of HBS is very complex, because their response not only depend on the amount of hydrate, but also on the type of pore habit (i.e., cementing, pore filling, or supporting matrix). It was observed that the behavior of HBS during hydrate dissociation (and after it) depends on stress level. For example, when hydrate dissociation took place at a low deviatoric stress (i.e. lower than the strength of the already dissociated sediment), the tendency of the sediment after dissociation was to harden. An opposite behavior was observed when the dissociation occurred at a higher deviatoric stress. It has also been suggested that hydrate bonding effects can be damaged during shearing (Uchida et al., 2012; Lin et al., 2015). The progressive stiffness degradation in tests involving HBS is generally very evident. Hydrate dissociation is also accompanied by profound changes in the sediment structure. Figure 2 shows schematically the expected changes in the soil structure that lead to the collapse compression deformations observed during dissociation under normally consolidated conditions (e.g., Fig. 1b). In summary, the mechanical response of HBS is highly non-linear, controlled by multiple inelastic phenomena that depends on hydrate saturation, sediment structure, and stress level. In the following section an advanced elastoplastic model for HBS is presented in detail.

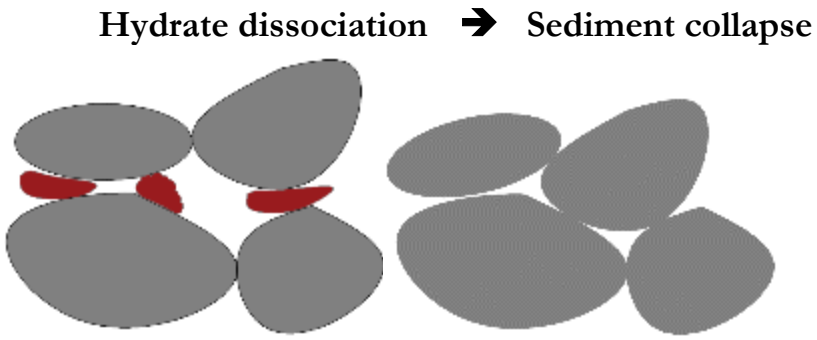

Figure 2) Schematic representation of the hydrate damaged during shearing; b) rearrangement of the HBS structure upon dissociation.

3 Mathematical framework

The proposed model contemplates the presence of two basics components: sediment skeleton and hydrate. The stress-partition concept proposed by Pinyol et al. (2003) for clayed cementing materials is adapted in this work for the case of HBS. Through this concept it is possible to compute the portion of the stresses that are carried by the hydrates and sediment matrix under different loading and hydrate saturation conditions, particularly during hydrate dissociation. Specific constitutive equations for these two basic structural components are proposed. For the sediment skeleton, a model based on critical state soil mechanics is adopted. The particular constitute equation adopted hereafter is based on a modification of the HISS elasto-plastic model (Desai et al., 1986). The proposed framework also incorporates sub-loading and dilation enhancement concepts. As for the hydrates, a damage model that considers the material degradation due to loading and dissociation is suggested.

3.1 Basic relationships

The stress-partition concept was adopted to develop the basic relationships. The total volume of the sample (V) can be computed as:

$$V = V_s + V_h + V_f \tag{1}$$

where V_s is the volume of sediment skeleton, V_h is the volume of hydrate, V_f is the volume occupied by the fluid in the pore space (Figure 3).

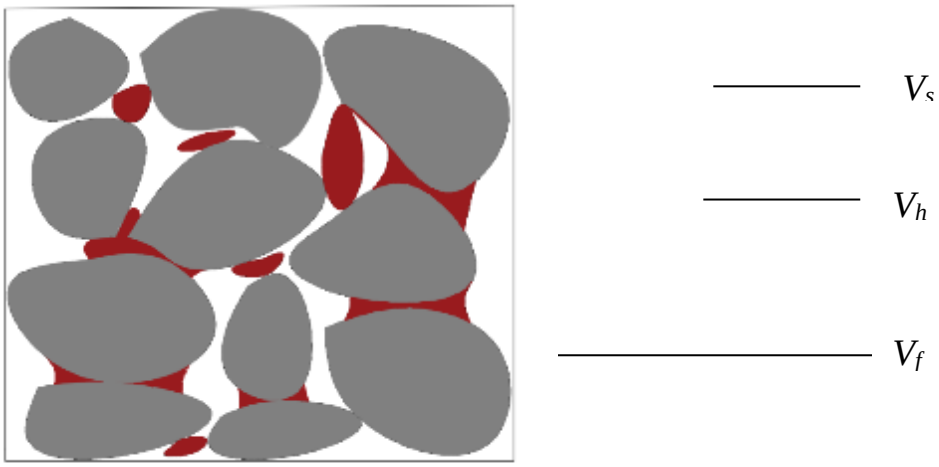

Figure 3. Schematic representation of a HBS.

Assuming that the grains are incompressible, the total volumetric strain can be defined as:

$$\varepsilon^{v} = -\frac{\Delta V_f}{V} - \frac{\Delta V_h}{V} \tag{2}$$

where the superscript *v* indicates volumetric strains. The volumetric strain of methane hydrate is computed as:

$$\varepsilon_h^{v} = -\frac{\Delta V_h}{V_h} \tag{3}$$

The deformation of hydrate can be defined locally through the following relationship:

$$-\frac{\Delta V_h}{V} = -\frac{\Delta V_h}{V_h}\frac{V_h}{V} = \varepsilon_h^{v} C_h \tag{4}$$

where C_h is the volumetric concentration of methane hydrate; which in turns is equal to the porosity (ϕ) times the hydrate saturation (i.e., $C_h = \phi S_h$). From equations (2) and (4), the total volumetric strain accounting for both the sediment skeleton (i.e., subscript *ss*) and the hydrate deformations can be calculated as:

$$\varepsilon^{v} = \varepsilon_{ss}^{v} + C_h \varepsilon_h^{v} \tag{5}$$

In a similar fashion the deviatoric strain can be computed as:

$$\varepsilon^{q} = \varepsilon_{ss}^{q} + C_h \varepsilon_h^{q} \tag{6}$$

The relationships that link hydrates and soil skeleton strains are proposed following an approach similar to Pinyol et al. (2003):

$$\varepsilon_h^{v} = \chi \varepsilon_{ss}^{v} \tag{7}$$

$$\varepsilon_h^q = \chi \varepsilon_{ss}^q \tag{8}$$

where χ is the strain partition variable that evolves during loading. The evolution law for this variable is presented in Section 3.2. From these equations, it can be anticipated that when the sediment skeleton deforms, the local hydrate strain reduces if χ decreases. Combining equations (5), (6), (7) and (8) leads to:

$$\varepsilon_h^v = \frac{\chi}{1 + C_h \chi} \varepsilon^v \tag{9}$$

$$\varepsilon_h^q = \frac{\chi}{1 + C_h \chi} \varepsilon^q \tag{10}$$

Equations (9) and (10) can also be written as a vector:

$$\boldsymbol{\varepsilon}_h = \frac{\chi}{1 + C_h \chi} \boldsymbol{\varepsilon} \tag{11}$$

In the following sections the specific constitutive models for the hydrate and sediment skeleton are discussed.

3.2. Constitutive model for methane hydrate

The damage theory is an appropriate framework to describe the degradation process of geomaterials subjected to loading. Isotropic scalar damage models track the degradation behavior of materials via damage variables. Loading degradation occurs when the stress state arrives to a predefined threshold. As mentioned above, previous studies suggested that hydrate effects can be damaged during shearing (Uchida et al., 2012; Lin et al., 2015). It is also assumed here that the material degradation takes place during hydrate dissociation. When the stresses are below a pre-established threshold, a linear elastic response of the material is assumed via the following relationships:

$$\boldsymbol{\sigma}_h = \mathbf{D}_{h0} \boldsymbol{\varepsilon}_h \tag{12}$$

where $\boldsymbol{\sigma}_h$ corresponds to the stresses taken by the hydrate and $\mathbf{D}_{h0}$ is the methane hydrate elastic constitutive matrix of the intact material, as follows:

$$\mathbf{D}_{h0}=\begin{bmatrix} K_{h0}+\frac{4}{3}G_{h0} & K_{h0}-\frac{2}{3}G_{h0} & K_{h0}-\frac{2}{3}G_{h0} & 0 & 0 & 0 \\ & K_{h0}+\frac{4}{3}G_{h0} & K_{h0}-\frac{2}{3}G_{h0} & 0 & 0 & 0 \\ & & K_{h0}+\frac{4}{3}G_{h0} & 0 & 0 & 0 \\ & \textit{Symetric} & & G_{h0} & 0 & 0 \\ & & & & G_{h0} & 0 \\ & & & & & G_{h0} \end{bmatrix} \tag{13}$$

where K_{h0} and G_{h0} are the bulk and shear moduli, respectively, of the intact hydrate. A logarithmic isotropic damage variable ($L:+\infty > L \geq 0$) is introduced to account for the damage induce by loading (Pinyol et al., 2003). The following expressions can be adopted for damaged states:

$$\boldsymbol{\sigma}_h = e^{-L}\mathbf{D}_{h0}\boldsymbol{\varepsilon}_h = \mathbf{D}_h\boldsymbol{\varepsilon}_h \tag{14}$$

where $\mathbf{D}_h$ is the methane hydrate constitutive matrix.

Adopting the damage model proposed by Carol et al. (2001), it is assumed that the material damage and the subsequent changes in L can be related to the variation in the energy (per unit of volume) stored in the hydrates. This energy can be defined as the elastic secant energy that would be recovered upon unloading; which, for triaxial conditions, is given by:

$$u_h = \frac{1}{2}\left(p_h\varepsilon_h^v + q_h\varepsilon_h^q\right) \tag{15}$$

The hydrate damage locus is defined by a threshold value 'r_0' of the secant elastic energy that can be represented by an ellipse in the 'p_h-q_h' space. The hydrate stiffness remains constant when the stresses are inside that ellipse. Loading damage takes place when the changes in the stress state is such that the secant elastic energy reaches r_0. In this case the damage variable L increases and the stiffness reduces. The damage evolution is determined by means of the function below (Carol et al., 2001):

$$r_{(L)} = r_0 e^{r_1 L} = u_h \tag{16}$$

where r_1 controls the damage rate. The consistency condition is adopted for defining the evolution law for L, Pinyol et al. (2003). Once the damaged variable L is defined, it is possible to introduce the evolution law for the partition variable, as follows:

$$\chi = \chi_0 e^{-\frac{L}{2}} \tag{17}$$

where χ_0 is an initial reference value assumed for the partition variable.

3.3 Constitutive model for the sediment

The constitutive model for the soil skeleton is based on a modified HISS framework. The constitutive equation incorporates sub-loading concepts, as well as hardening and dilation enhancement mechanisms associated with the presence of hydrates in the sediments. The main components of this mode were presented in a previous report (i.e. Sanchez, 2015), only a brief summary is presented here. The modified sub-loading yield surface is given by:

$$F_s = \frac{a}{M^2} q_{ss}^{\ 2} - 9\gamma \left\{ \left(p_{ss}^{'} \right)^2 - \left(p_{ss}^{'} \right)^n \left[R\left(p_c + p_d \right) \right]^{2-n} \right\} \tag{18}$$

where a and γ are model constants; n is the parameter related to the transition from compressive to dilative behavior; p_{ss}' and q_{ss} are the mean effective and deviatoric stresses, respectively, both associated with the sediment skeleton; M is the slope of critical line in the q_{ss}-p_{ss}' space; and p_c is the effective pre-consolidation pressure. The isotropic expansion of the yield surface associated with the presence of hydrates is controlled by the hardening parameter 'p_d' (Uchida et al., 2012):

$$p_d = \alpha \left(\chi C_h \right)^{\beta} \tag{19}$$

where α and β are constants that describe the degree of hydrate contribution to the hardening law. In Eq. (18) R is the sub-loading surface ratio. As suggested by Hashiguchi et al. (1977), it is assumed that $0 < R \leq 1$. The changes in R are defined through the following evolution law (Uchida et al., 2012):

$$dR = -\eta \ln R \left| d\varepsilon^p \right| \tag{20}$$

where $|d\varepsilon^p|$ is the norm of the plastic strain vector and η is a sub-loading parameter that controls the plastic deformations inside F_b, where F_b is the external or boundary yield surface. The term between brackets in Eq. (18) is called effective hardening parameter (i.e., $H=R(p_c+p_d)$).

3.4 Final stress-strain relationships

To obtain the expressions relating the external effective stress $\boldsymbol{\sigma}'$ with the two stress components, the principle of virtual work is advocated, which for triaxial conditions can be written as (Pinyol et al., 2003):

$$p^{'} d\varepsilon^v + q d\varepsilon^q = p_{ss}^{'} d\varepsilon^v + q_{ss} d\varepsilon^q + p_h C_h d\varepsilon_h^v + q_h C_h d\varepsilon_h^q \tag{21}$$

After replacing equations (9) and (10) into equation (21) leads to:

$$p^{'} d\varepsilon^v + q d\varepsilon^q = p_{ss}^{'} d\varepsilon^v + q_{ss} d\varepsilon^q + p_h C_h \frac{\chi}{1+C_h\chi} d\varepsilon^v + q_h C_h \frac{\chi}{1+C_h\chi} d\varepsilon^q \tag{22}$$

Considering that the equation above is valid for any external strain:

$$p' = p'_{ss} + \frac{C_h \chi}{1 + C_h \chi} p_h \tag{23}$$

$$q = q_{ss} + \frac{C_h \chi}{1 + C_h \chi} q_h \tag{24}$$

For a given C_h the redistribution of external stress between hydrates and soil skeleton is given by χ. When χ decreases (i.e., when damage is taking place), stresses are progressively transferred from the hydrate to the sediment matrix. It is also observed that during dissociation the stress are transfer from the hydrates to the sediment skeleton and when the hydrates fully dissociate, the external stresses are equal to the soil skeleton (i.e., as expected there is no contribution from the hydrates).

Considering equations (23) and (24), the total stress can be expressed as follows.

$$d\boldsymbol{\sigma}' = d\boldsymbol{\sigma}'_{ss} + \frac{C_h \chi}{1 + C_h \chi} d\boldsymbol{\sigma}_h \tag{25}$$

The constitutive equations quoted above provide the relationships between the external stresses in terms of hydrate and soil matrix stresses. These equations can be integrated numerically as suggested in Pinyol et al. (2007).

4 Model Application

The performance of the model presented in Section 3 was compared against available experimental data (most of it published very recently) involving hydrate dissociation.

The same parameters for the hydrate (e.g, K_h, G_h) were assumed in all the cases analyzed in the following sections. The hydrate parameters were obtained from the literature (e.g. Miranda and Matsuoka, 2008), and they are listed in the tables prepared for each one of the cases presented below. As for the model related to the sediment skeleton, an ellipse (as in the MCC model) was adopted in all the cases. This decision was taken for the sake of simplicity. Furthermore, typical elastic parameters for the sediment skeleton were adopted (e.g, K_{ss}, G_{ss}). It is also worth mentioning that the main aim of the modeling was not to exactly reproduce the experimental behavior, but to check whether or not the suggested approach was able to capture the main features of HBS behavior observed in these experiments.

4.1 Effect of hydrate dissociation on HBS behavior under triaxial conditions

The tests conducted by Hyodo et al. (2014) were selected to study the effect of hydrate dissociation under triaxial conditions. The main information about the samples and tests details were introduced in Section 1. Table 1 presents the main tests conditions related to these experiments.

Table 1. Test conditions of methane hydrate dissociation tests. Section 4.4.

Consolidation condition	σ'_c (MPa)	S_h (%)	Porosity (%)	Test Nº	Remarks
Isotropic	5	48.7	40.4	1	Dissociation→Shear
Isotropic	5	47.4	39.9	2	Shear1%→Dissociation→Shear
Isotropic	5	47.9	39.8	3	Shear5%→Dissociation→Shear

These tests provide very useful information about the effect of hydrate dissociation at two stages of shearing. When the dissociation was induced at ε_a=1%, the stress conditions were quite far from the failure of the dissociated sediment (i.e., the deviatoric stress of this sample at ε_a=1% was 8.4 MPa, while the strength at failure of the already dissociated sample was around 10 MPa, Fig. 1a). However, when the hydrate dissociation started at ε_a=5% the deviatoric stress (i.e. q≈12 MPa) was higher than strength of the dissociated sediment. This made difficult to maintain the constant stress condition during dissociation, because the sample failed and the deviatoric stress reduced tending to the strength of the dissociated sample (i.e., q≈10 MPa). As it can be seen, these were quite complex experiments. An attempt was made in this work to simulate them as close as possible to the reported test protocols (Hyodo et al., 2014)

The modeling of these experiments was approached as follows: i) first the test related to the already dissociated sediment was simulated (using typical reported parameters for this type of material, i.e. sand); then, ii) the test related to the dissociation at ε_a=1% was studied and used to adjust the model parameters for the HBS case; and, finally iii) the test involving hydrate dissociation at an initial ε_a=5% was simulated to validate the proposed model under these particular conditions. Table 2 lists the main parameters selected for the modeling.

Figures 4, 5 and 6 present the comparisons between experiment and model results for the three cases discussed above. As for the already dissociated sample (Fig. 4), quite good agreements were obtained in terms of deviatoric stress and volumetric behavior. In particular, the model manages to replicate well the maximum stress, but slightly under-predicts the maximum volumetric strain. Figure 5 presents the experimental and numerical results related to the sample at which dissociation is induced at ε_a=1%. In addition to the external deviatoric stresses (i.e., the one to be compared against the experimental observations) the stresses carried by the hydrate and the sediment skeleton computed by the model are also included in this figure.

Table 2. Parameters adopted in the modeling of HBS specimens. Section 4.1.

Properties	Shear after dissociation	Dissociation induced at ε_a= 1%	Dissociation induced at ε_a= 5%
M	1.17	1.17	1.17
λ	0. 12	0.12	0.12
κ	0.002	0.002	0.002
p_c (MPa)	11.5	11.5	11.5
n	3	3	3
a	1	1	1
γ	-1/9	-1/9	-1/9
C_h	0	0.195	0.195
α	-	16	16
β	-	1.0	1.0
r_1	-	2.9	2.9
r_0	-	1e-5	1e-5
η	-	35	35
χ_0	-	3	3
K_h (MPa)	9600	9600	9600
G_h (MPa)	4300	4300	4300

Initially the stresses increased progressively in the sediment skeleton and hydrate. Then, during the stage of hydrate dissociation at constant external stress conditions, the stresses in the hydrate were progressively decreasing and transferred to the soil skeleton. This is why the stress in the sediment increased during the constant stress conditions. The external stress is solely supported by the soil skeleton at the end of the dissociation process. The deviatoric stress increased in the subsequent shearing, until reaching the strength of the already dissociated sediment. The model captures very satisfactorily the main trends observed in this experiment, particularly: the degradation in stiffness during the initial loading stage, the (average) deviatoric stress during dissociation, and the maximum final deviatoric stress after dissociation. However, the experimental deviatoric stress at ε_a=1% is a bit higher than the one computed by the model, and the axial strains observed during dissociation are larger than the simulated ones. Note that in any case, the volumetric deformations during dissociation are well reproduced by the model. The model slightly under-predicts the ε_v at advanced stages of the experiment (i.e., ε_a>12%). At that final stages of shearing, the three yield surfaces considered in this model coincided in one, and the stress state is on the summit of that ellipse. Therefore, according to the model there are not changes in plastic volumetric strains (i.e., $d\varepsilon^p_v$=0) and ε^p_v remains fairly constant. In this way the model simulates the material failure (i.e., continuous deformations at constant deviatoric stress). More details about how the different mechanisms adopted in this model work are presented in the following case.

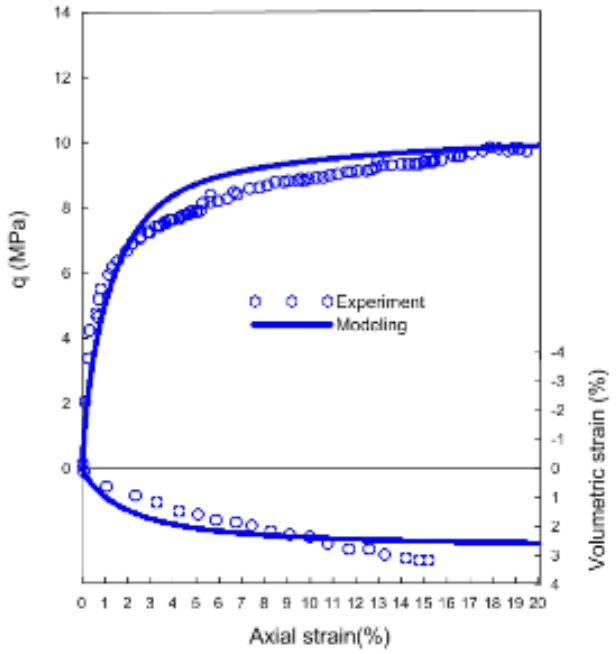

Figure 3. Experimental and modeling results for drained triaxial tests: already dissociated sediment. Experimental data from Hyodo et al. (2014).

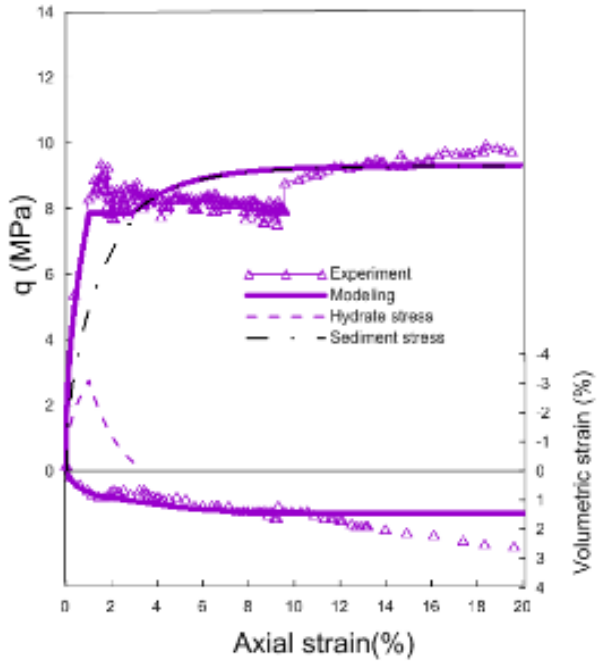

Figure 4. Experimental and modeling results for drained triaxial tests: dissociation induced at ε_a=1%. Experimental data from Hyodo et al. (2014).

Once the model parameters were calibrated using the two previous cases, the ability of the constitutive equation to predict the HBS behavior under dissociation was checked against the third test. Fig. 5 presents the comparisons between the experimental results and the model predictions for the case in which the hydrate is dissociated under load and at and initial ε_a=5%.

The model results are also quite satisfactory in this case, the main tendencies observed in this experiment are well captured by the model. However, the peak deviatoric stress is slightly over-predicted by the model. There are also some differences between the model predictions and the reported experimental data in terms of volumetric behavior. Surprisingly, it was observed that there was not volume change at the end of this test, because an apparent dilation during dissociation compensate the initial positive volumetric strains. This final dilation seems a bit strange, the tendency during dissociation at high stresses should be to contract, because the sediment structure should tend to a more compact state as the hydrates disappear. The positive ε_v predicted by the model during dissociation are related to the volumetric compression plastic strains induced by the collapse of the sediment structure during hydrate dissociation (as shown in Fig. 1b, and illustrated in Fig. 2). This structure-collapse behavior is explained in more detail in Section 4.2.

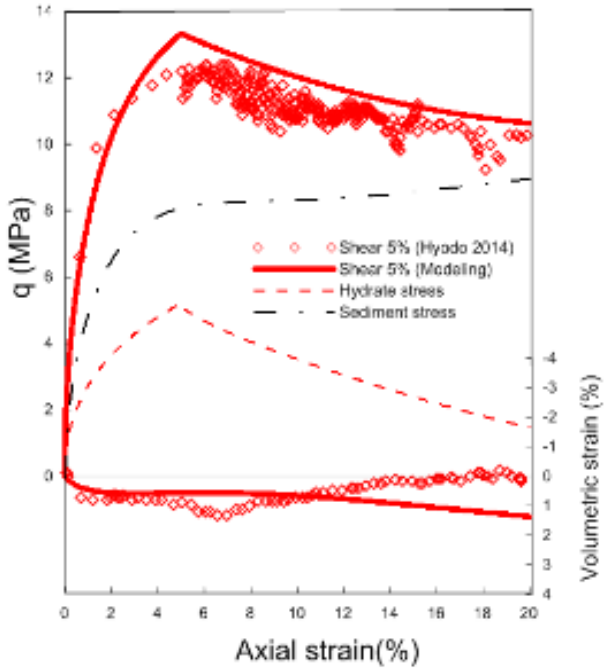

Figure 5. Experimental and modeling results for drained triaxial tests: dissociation induced at ε_a=5%. Experimental data from Hyodo et al. (2014).

Hyodo et al. (2014) had problems to hold the deviatoric stress constant during dissociation in this test (i.e., as it was done in the previous one). The progressive degradation of the HBS structure during hydrate dissociation made impossible to hold the (high) deviatoric stress applied just before dissociation (i.e., at ε_a=5%). The stress carried by the hydrate (dash line) was gradually transferred to the sediment skeleton during dissociation, and the global deviatoric stress decreased progressively until reaching the maximum strength associated with the already dissociated sediment. At the end of the test, the model predicts that part of the stresses are still carried by the hydrates, this is in line with the reported experimental data indicating that not all the hydrates dissociated at the final axial strain (i.e., ε_a=20%).

Figure 6 shows additional information about this modeling. Figure 6a presents the q-ε_a plot extended until full dissociation. As discussed before, during dissociation the bearing capacity of the hydrates decreased and the stress were gradually transferred to the sediment. The model predicts that at advanced stages of shearing and hydrate dissociation all the external stresses are supported by the sediment skeleton only. Note that a linear decrease of S_h was adopted in the modeling of these experiments. The effective hardening parameter ($H=R(p_c+p_d)$) always increased (Fig. 6b). This implies that F_s kept expanding during the whole test. The variable R always increased during the simulation as well (Fig. 6b). The increase in H (i.e. hardening of the sediment skeleton) observed at advanced stages of the experiment was induced by the volumetric-collapse-compression strains discussed above; which compensated the decrease of p_d during hydrate dissociation. Figures 6c presents the three initial yield surfaces (i.e., F, F_s, and F_b) considered in this model at the start of the test. Figure 6d presents again these three yield surfaces at two different stages: i) at ε_a=15.3%, i.e. when the sub-loading yield surface reached the boundary one (F is still inside F_b=F_s, because p_d did not vanish totally at this stage); and ii) at the end of the test, when the three yield surfaces coincided in one.

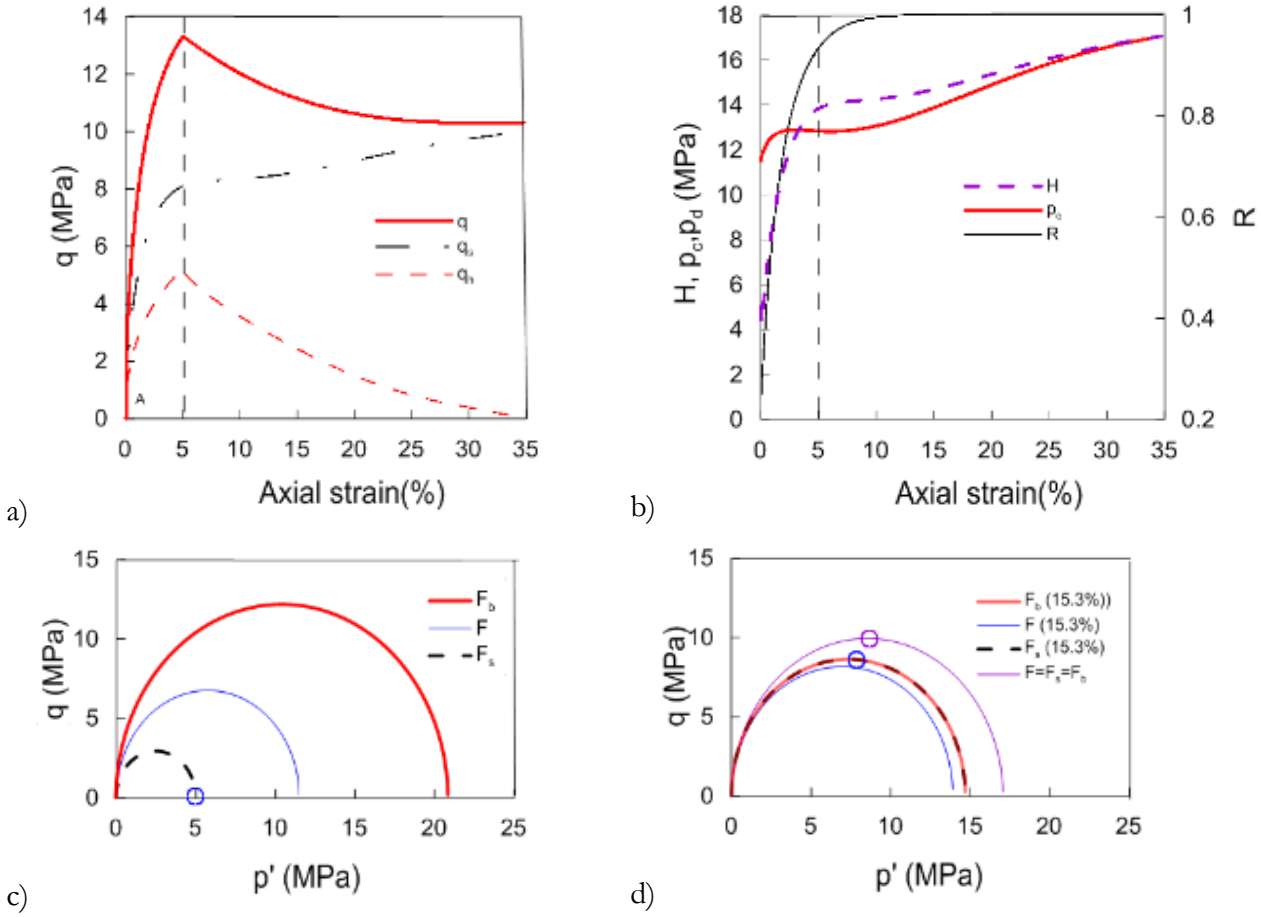

Figure 6. Additional modeling information for the test dissociation starting at ε_a=5%: a) extended stress-strain behavior; b) hardening variables, c) yield surfaces at the beginning of the experiment; and c) yield surfaces at an intermediate stage of shearing and at the end of test.

This model has not only reproduced and predicted quite satisfactorily the behavior observed in this study, but it has also allowed explaining the main features and trends of material behavior observed during the tests. In the experiments, the dissociation was induced by heating, Hyodo et al. (2014). Thermal effects were not modeled in this analysis, this seems a reasonable assumption as the main focus here was on the influence of hydrates dissociation on material behavior. It also seems that temperature may have a small influence on the overall mechanical behavior of the specimen in this type of experiment. A more sophisticated analysis can certainly be done in the future incorporating thermal effects. The inclusion of temperature could also help to reproduce these experiments more closely.

4.6 Effect of hydrate dissociation on HBS behavior under oedometric conditions

The experimental data studied in this report corresponds to tests reported by Santamarina et al. (2015). Two natural core samples were extracted using Pressure Core Characterization Tools (PCCTs) and tested under oedometric conditions. General information about this research was presented in Section 2.2. The test presented in Fig. 1b) plus another one with a lower hydrate saturation are simulated in this section. The parameters reported for the dissociated sediment (i.e. a silty sand) were adopted in the simulations (Santamarina et al., 2015). The selected parameters are listed in Table 3.

Table 3. Parameters adopted in the modeling of HBS specimens in Section 4.6

Properties	**core 8P**	**core 10P**
M	1.07	1.07
λ	0.605	0.12
κ	0.065	0.04
p_c (MPa)	2.32	3.5
n	3	3
a	1	1
γ	-1/9	-1/9
C_h	0.102	0.3605
α	6	12.5
β	1.0	1.0
r_1	30	10
r_0	1e-6	1e-6
η	15	1.5
χ_0	1	3
K_h (MPa)	9600	9600
G_h (MPa)	4300	4300

Figure 7a shows the comparison between experimental and modeling results for the sample coded as ‘core 8P’ with S_h=18%. Prior to hydrate dissociation the specimen was loaded up to a vertical stress σ'_v=6 MPa and then unloaded back to σ'_v=3 MPa to study the stress-volume response of HBS.

Under this over-consolidated conditions, hydrate dissociation was induced. Once the hydrate fully dissociated, the sample was subjected to loading-unloading cycles with a maximum σ'_v=9 MPa. Figure 7b presents the results related to specimen coded as 'core 10P', initial S_h=74%. This sample was loaded until σ'_v=3 MPa, at this normally-consolidated conditions, the effective stress was hold constant and hydrate dissociation was induced. After hydrate dissociation, the sample was loaded up to σ'_v=9 MPa and then unloaded.

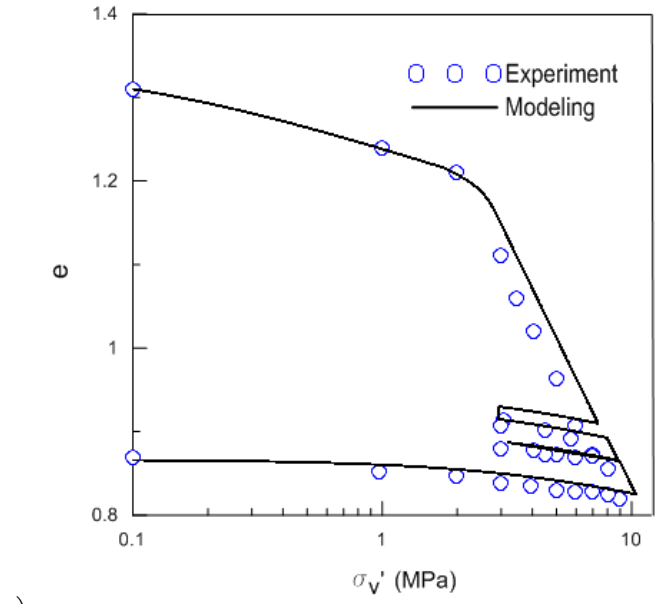

a)

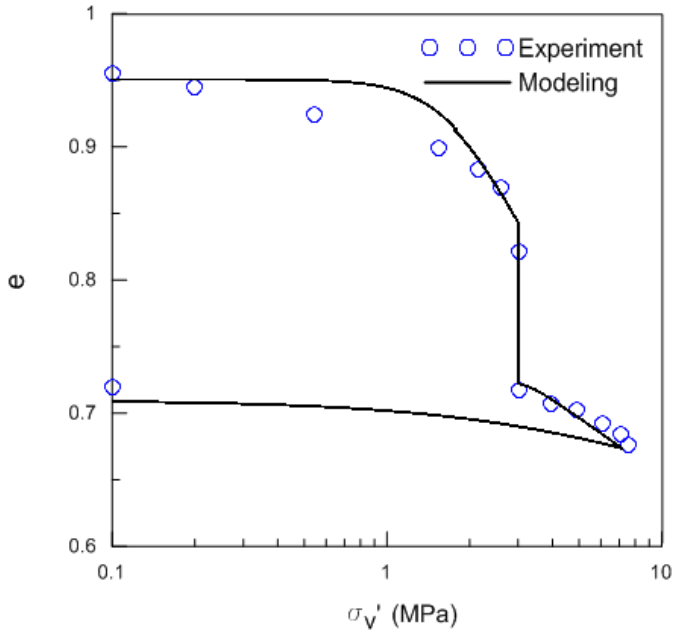

b)

Figure 7. Behavior during dissociation of natural HBS specimens under oedometric conditions: a) core 8P; and b) core 10P. Experimental data from (Santamarina et al., 2015).

The model managed to capture very satisfactorily the main trends observed in both tests. The yield stress and unloading-reloading behavior are quite well modeled in both specimens. The model slightly over-predicts the initial stiffness of the core-10P. It is worth to highlight the model ability to reproduce the difference in volumetric strains observed during dissociation at constant stress in these two tests. In the case of core-8P, the collapse-compression behavior is significantly less marked than in core-10P, where the rearrangement of the HBS structure is huge during dissociation. The main reasons behind this different behavior can be related to: i) hydrate saturation is much smaller in core-8P than core-10P (i.e., S_h=18% for core-8P, and S_h=74% for core-10P); ii) the vertical stress at which hydrates are dissociated is lower and the dissociation took place under over-consolidated conditions, therefore the effect of confinement on the re-accommodation of the sediments particles is less significant; and iii) this sample was previously loaded up to a very high effective vertical stress (i.e. σ'_v=6MPa) that degraded the bonding effect of the hydrate and induced important changes in the sediment structure previous to dissociation.

Figure 8 presents the evolution of σ'_v calculated by the model in the soil skeleton and hydrate, together with the global (or external) one for the case of core-8P. An important portion of the stress increase is taken by the hydrate at the beginning of the experiment, i.e. path 'A-B'. Note that S_h is very high in this case (i.e., S_h=74%) and therefore an important bearing contribution from the hydrate can be anticipated. Upon dissociation at constant effective stress, the load is gradually transferred from the hydrate to the sediment skeleton and significant plastic volumetric strains are computed by the model, i.e. path 'B-C'. After full dissociation, the stresses are supported by the soil skeleton only, and the subsequent loading ('C-D') and unloading ('D-E') steps are controlled by the properties of the already dissociated sediment.

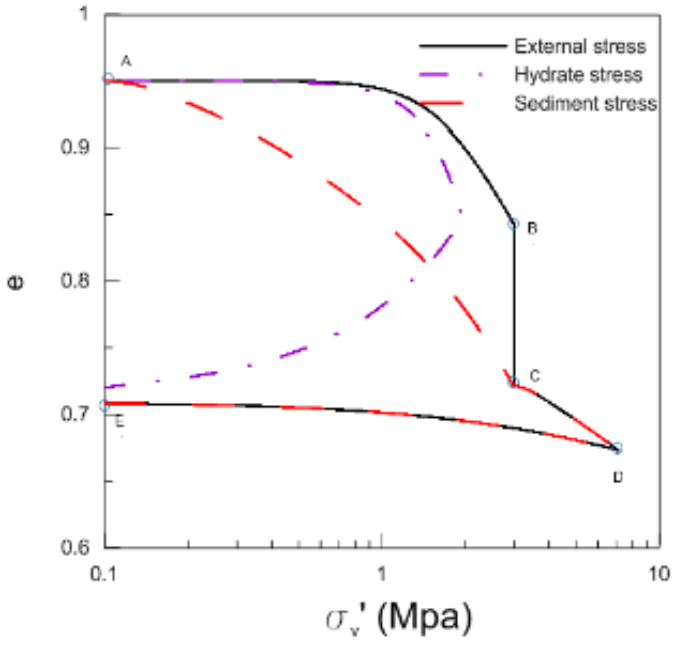

Figure 8. Additional modeling information for the test related to core 10P: a) vertical stresses computed by the model during loading.

Figure 9 shows that the hardening enhancement effect reduces progressively during loading and it disappears during dissociation. The effective hardening parameter *H* increases during loading and remained unchanged upon unloading.

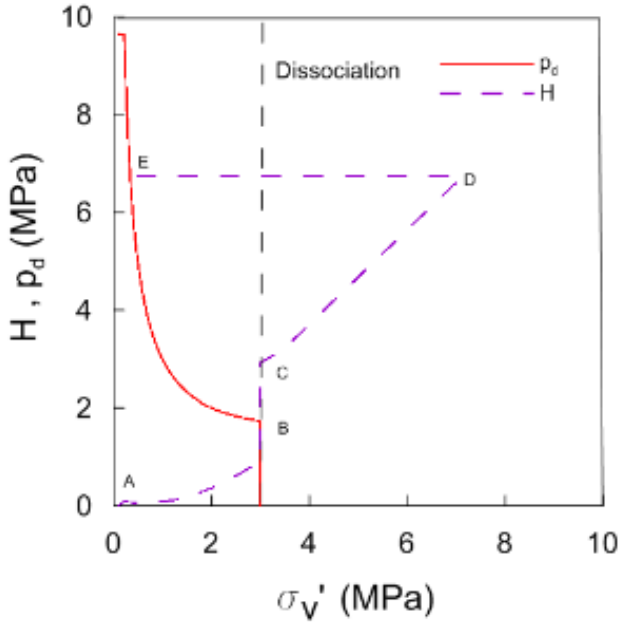

Figure 9. Additional modeling information for the test related to core 10P: hardening variables

5. CONCLUSIONS

Experimental observations have shown that the presence of hydrates impacts on different aspects of sediment behavior, amongst others: stiffenss, peak stress, softening behavior and dilation. It has been observed that these features of soil behavior depend on hydrate saturation as well. Hydrates also contribute to support the applied external stresses. Furthermore, during dissociation important changes in the mechanical behavior of HBS and soil structure have been observed. The model proposed in this work encompasses different inelastic mechanisms to describe these complex features of HBS behavior. The concept of stress partition was incorporated into the model to estimate the amount of stresses that are supported by the hydrate and the soil skeleton at different stages of loading and dissociation. A damage model was adopted to describe the behavior of hydrate during loading, while the HISS elastoplastic model was selected for the sediment skeleton. The HISS model is a versatile mechanical constitutive law based on critical state soil mechanics. The proposed framework also incorporates sub-loading and hydrate enhancement mechanisms.

The performance of the model when compared against published experimental data involving hydrate dissociation under loading. The model was able to reproduce quite satisfactorily the main features of soil behavior observed in these tests as, for example: the enhancement in stiffness and strength induced by the presence of the hydrate, stiffenss degradation during shearing, soil dilatancy, and the volumetric soil collapse compression observed during hydrate dissociation at

constant stresses. The model also assisted to interpret the behavior of this complex material during loading and dissociation.

6. References

Carol I, Rizzi E, Willam K. On the formulation of anisotropic elastic degradation. I. Theory based on a pseudo-logarithmic damage tensor rate. International Journal of Solids and Structures. 2001;38(4):491-518.

Desai CS, Somasundaram S, Frantziskonis G. A hierarchical approach for constitutive modelling of geologic materials. International Journal for Numerical and Analytical Methods in Geomechanics. 1986;10(3):225-57.

Hashiguchi K. Ueno M. Elasto-plastic constitutive laws of granular materials, Constitutive Equations of Soils. Proc. Conf. Soil Mech. Found. Engrg., 9th ICSMFE, Tokyo. 1977:73-82.

Hyodo M, Li Y, Yoneda J, Nakata Y, Yoshimoto N, Nishimura A. Effects of dissociation on the shear strength and deformation behavior of methane hydrate-bearing sediments. Marine and Petroleum Geology. 2014;51:52-62.

Lin JS, Seol Y, Choi JH. An SMP critical state model for methane hydrate-bearing sands. International Journal for Numerical and Analytical Methods in Geomechanics. 2015.

Miranda CR, Matsuoka T. First-principles study on mechanical properties of CH4 hydrate. Proceedings of the 6th International Conference on Gas Hydrates, 2008.

Sanchez (2015). "THCM Coupled Model For Hydrate-Bearing Sediments: Data Analysis and Design of New Field Experiments (Marine and Permafrost Settings)". DOE Quarterly Research Performance Progress Report (Period ending 06/30/2015).

Santamarina JC, Dai S, Jang J, Terzariol M. Pressure core characterization tools for hydrate-bearing sediments. Sci. Drill. 2012;14(4).

Santamarina JC, Dai S, Terzariol M, Jang J, Waite WF, Winters WJ, Nagao J, Yoneda J, Konno Y, Fujii T, Suzuki K. Hydro-bio-geomechanical properties of hydrate-bearing sediments from Nankai Trough. Marine and Petroleum Geology. 2015.

Pinyol, N.; Vaunat, J.; Alonso, E.E. A constitutive model for soft clayey rocks that includes weathering effects. Géotechnique, 2007; 57, 2, 137-151.

Uchida S, Soga K, Yamamoto K. Critical state soil constitutive model for methane hydrate soil. Journal of Geophysical Research: Solid Earth (1978–2012). 2012; 117(B3).

PRODUCTS

Publications – Presentations:

- A conference was presented at the 'XV Pan-American Conference on Soil Mechanics and Geotechnical Engineering, hold in Buenos Aires, 15th to 18th November 2015 Title: "Mechanical Modeling of Gas Hydrate Bearing Sediments Using an Elasto-Plastic Framework". Authors: Xuerui Gai, and M. Sanchez.
- A session on "Hydrate bearing sediments: characterization, modeling and implications on geohazard and gas production", was organized during the AGU Fall meeting 2015, San Francisco, 14th to 18th December 2015. Marcelo Sanchez was one of the session conveners.
- A journal paper has been accepted (is under 2nd review, minor changes) for publication in Environmental Geotechnics. Title: "Mechanical Modeling of Gas Hydrate Bearing Sediments Using an Elasto-Plastic Framework". Authors: Xuerui Gai, and M. Sanchez.
- A journal paper was submitted for publication. Title: "A Constitutive Mechanical Model for Gas Hydrate Bearing Sediments Incorporating Inelastic Mechanisms". Authors: M. Sanchez, Xuerui Gai, and J.Carlos Santamarina.

Website: Publications (for academic purposes only) and key presentations are included in: http://engineering.tamu.edu/civil/people/msanchez

Technologies or techniques: None at this point.

Inventions, patent applications, and/or licenses: None at this point.

Other products: None at this point.

PARTICIPANTS

Research Team: The current team is shown next.

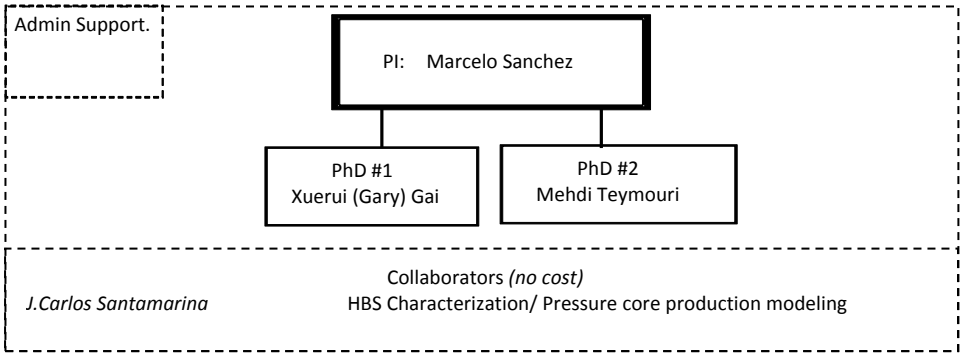

IMPACT

- We can already highlight the computational platform extensively validated in a wide range of coupled thermo-hydro-chemo-mechanical coupled problems (CB_Hydrate).

CHANGES/PROBLEMS:

None so far.

SPECIAL REPORTING REQUIREMENTS:
Nothing to report

BUDGETARY INFORMATION:

Grant No.DE-FE0013889										**EXHIBIT 2- COST PLAN/STATUS**								
TEES Project 32525-C3870 CE																		
COST PLAN/STATUS																		
				Budget Period 1								**Budget Period 2**						
	Q1		**Q2**		**Q3**		**Q4**		**Q1**		**Q2**		**Q3**		**Q4**		**Q1**	
	Enter date range		**Enter date range**		**Enter date range**		**Enter date range**		**Enter date range**		**Enter date range**		**Enter date range**		**Enter date range**		**Enter date range**	
Baseline Reporting Quarter	**10/1/13-12/31/13**		**01/01/14-03/31/14**		**04/01/14-06/30/14**		**07/01/14-9/30/14**		**10/1/14-12/31/2014**		**01/01/15-03/31/15**		**04/01/15-06/30/15**		**07/01/15-9/30/15**		**10/1/15-12/31/2015**	
	Q1	**Cumulative Total**	**Q2**	**Cumulative Total**	**Q3**	**Cumulative Total**	**Q4**	**Cumulative Total**	**Q1**	**Cumulative Total**	**Q2**	**Cumulative Total**	**Q3**	**Cumulative Total**	**Q4**	**Cumulative Total**	**Q1**	**Cumulative Total**
Baseline Cost Plan	$ 40,500.00	$40,500.00	$ 40,500.00	$ 81,000.00	$ 40,500.00	$121,500.00	$ 92,180.00	$ 213,680.00	$ 27,600.00	$241,280.00	$ 27,600.00	$ 268,880.00	$ 27,600.00	$ 296,480.00	$ 92,080.00	$ 388,560.00	$ -	$388,560.00
Federal Share	$ 40,500.00	$40,500.00	$ 40,500.00	$ 81,000.00	$ 40,500.00	$121,500.00	$ 92,180.00	$ 213,680.00	$ 27,600.00	$241,280.00	$ 27,600.00	$ 268,880.00	$ 27,600.00	$ 296,480.00	$ 92,080.00	$ 388,560.00	$ -	$388,560.00
Non-Federal Share	$ 11,223.00	$11,223.00	$ 11,223.00	$ 22,446.00	$ 11,223.00	$ 33,669.00	$ 11,223.00	$ 44,892.00	$ 11,223.00	$ 56,115.00	$ 11,223.00	$ 67,338.00	$ 11,223.00	$ 78,561.00	$ 11,223.00	$ 89,784.00	$ -	$ 89,784.00
Total Planned	$ 51,723.00	$51,723.00	$ 51,723.00	$ 103,446.00	$ 51,723.00	$155,169.00	$103,403.00	$ 258,572.00	$ 38,823.00	$297,395.00	$ 38,823.00	$ 336,218.00	$ 38,823.00	$ 375,041.00	$103,303.00	$ 388,560.00	$ -	$388,560.00
Actual Incurred Costs	$ 5,301.83	$ 5,301.83	$ 13,764.34	$ 19,066.17	$ 33,827.48	$ 52,893.65	$ 51,567.77	$ 104,461.42	$ 80,352.17	$184,813.59	$ 24,626.18	$ 209,439.77	$ 19,260.19	$ 228,699.96	$ 29,858.73	$ 258,558.69	$ 13,074.57	$271,633.26
Federal Share	$ 3,335.02	$ 3,335.02	$ 9,848.68	$ 13,183.70	$ 10,170.37	$ 23,354.07	$ 58,205.62	$ 81,559.69	$ 92,208.79	$173,768.48	$ 31,359.66	$ 205,128.14	$ 19,260.19	$ 224,388.33	$ 29,812.17	$ 349,425.73	$ 4,088.61	$353,514.34
Non-Federal Share	$ 5,182.96	$ 5,182.96	$ 20,751.77	$ 25,934.73	$ 20,743.19	$ 46,677.92	$ 29,262.19	$ 75,940.11	$ -	$ 75,940.11	$ -	$ 75,940.11	$ 8,833.66	$ 84,773.77	$ -	$ 84,773.77	$ -	$ 84,773.77
Total Incurred costs	$ 8,517.98	$ 8,517.98	$ 30,600.45	$ 39,118.43	$ 30,913.56	$ 70,031.99	$ 87,467.81	$ 157,499.80	$ 92,208.79	$249,708.59	$ 31,359.66	$ 281,068.25	$ 28,093.85	$ 309,162.10	$ 29,812.17	$ 434,199.50	$ 8,985.96	$271,633.26
Varience	$ 43,205.02	$43,205.02	$ 21,122.55	$ 64,327.57	$ 20,809.44	$ 85,137.01	$ 15,935.19	$ 101,072.20	$(53,385.79)	$ 47,686.41	$ 38,823.00	$ 55,149.75	$ 10,729.15	$ 65,878.90	$ 73,490.83	$ (45,639.50)	$ (8,985.96)	$116,926.74
Federal Share	$ (1,966.81)	$ (1,966.81)	$ (3,915.66)	$ (5,882.47)	$ (23,657.11)	$ (29,539.58)	$ 6,637.85	$ (22,901.73)	$ 11,856.62	$ (11,045.11)	$ 6,733.48	$ (4,311.63)	$ -	$ (4,311.63)	$ 4,358.19	$ 46.56	$ 4,358.19	$ 4,404.75
Non-Federal Share	$ 6,040.04	$ 6,040.04	$ (9,528.77)	$ (3,488.73)	$ (9,520.19)	$ (13,008.92)	$ (40,485.19)	$ (53,494.11)	$ 11,223.00	$ (42,271.11)	$ 6,733.48	$ (35,537.63)	$ 2,389.34	$ (33,148.29)	$ 11,223.00	$ (21,925.29)	$ -	$ (21,925.29)
Total Varience	$ 4,073.23	$ 4,073.23	$ (13,444.43)	$ (9,371.20)	$ (33,177.30)	$ (42,548.50)	$ (33,847.34)	$ (76,395.84)	$ 23,079.62	$ (53,316.22)	$ 13,466.96	$ (39,849.26)	$ 2,389.34	$ (37,459.92)	$ 15,581.19	$ (21,878.73)	$ 4,358.19	$ (17,520.54)

National Energy Technology Laboratory

626 Cochrans Mill Road
P.O. Box 10940
Pittsburgh, PA 15236-0940

3610 Collins Ferry Road
P.O. Box 880
Morgantown, WV 26507-0880

13131 Dairy Ashford Road, Suite 225
Sugar Land, TX 77478

1450 Queen Avenue SW
Albany, OR 97321-2198

Arctic Energy Office
420 L Street, Suite 305
Anchorage, AK 99501

Visit the NETL website at:
www.netl.doe.gov

Customer Service Line:
1-800-553-7681